



Construction of heterostructured $\text{ZnIn}_2\text{S}_4/\text{NH}_2\text{-MIL-125(Ti)}$ nanocomposites for visible-light-driven H_2 production

Hong Liu*, Jiang Zhang, Dan Ao

Department of Chemical Engineering, School of Environmental and Chemical Engineering, Shanghai University, 99 Shangda Road, Shanghai 200444, PR China

ARTICLE INFO

Keywords:

Metal-organic frameworks

ZnIn_2S_4

Photocatalysis

Hydrogen production

ABSTRACT

Metal-organic frameworks (MOFs) have been attracted considerable attention in the field of energy generation and environmental remediation. However, the functionalization and diversification of MOFs are still challenging and imperative for the development of highly active MOF-based materials. In this article, a series of heterostructured $\text{ZnIn}_2\text{S}_4/\text{NH}_2\text{-MIL-125(Ti)}$ nanocomposites with different $\text{NH}_2\text{-MIL-125(Ti)}$ contents were fabricated via a facile solvothermal method. The photocatalytic activities of the obtained samples were evaluated by the photocatalytic H_2 production under visible-light illumination ($\lambda > 420 \text{ nm}$). The results showed that the ZnIn_2S_4 nanosheets were highly dispersed on the surface of $\text{NH}_2\text{-MIL-125(Ti)}$. The $\text{ZnIn}_2\text{S}_4/\text{NH}_2\text{-MIL-125(Ti)}$ photocatalysts displayed higher photocatalytic activity than the pristine components for H_2 production. The optimal content of $\text{NH}_2\text{-MIL-125(Ti)}$ was about 40 wt% and the corresponding photocatalytic H_2 production rate was $2204.2 \mu\text{mol h}^{-1} \text{g}^{-1}$ (with an apparent quantum efficiency of 4.3% at 420 nm), which was 6.5 times higher than that of pure ZnIn_2S_4 . The enhanced photocatalytic activity of $\text{ZnIn}_2\text{S}_4/\text{NH}_2\text{-MIL-125(Ti)}$ composites should be attributed to the well-matched band structure and intimate contact interfaces between ZnIn_2S_4 and $\text{NH}_2\text{-MIL-125(Ti)}$, which led to the effective transfer and separation of the photogenerated charge carriers. Moreover, the $\text{ZnIn}_2\text{S}_4/\text{NH}_2\text{-MIL-125(Ti)}$ nanocomposites showed excellent stability during the photocatalytic reactions under visible light. Therefore, these kinds of MOF-based composites have great potentiality in energy conversion fields.

1. Introduction

Photocatalytic H_2 production from water splitting utilizing solar energy has attracted increasing attention because of global energy crisis and environmental pollution problems. So far, a variety of semiconductor materials including metal oxides [1,2], sulfides [3,4], oxynitrides [5] and metal-free semiconductors [6,7] have been explored for photocatalytic hydrogen production. Among all the already reported photocatalysts, metal sulfides are regarded as good candidates for photocatalytic hydrogen production due to their strong absorption in the visible light region. ZnIn_2S_4 is a ternary chalcogenide which has a suitable bandgap (2.34–2.48 eV) well corresponding to the visible light absorption [8–10]. ZnIn_2S_4 exhibits two distinct polymorphs based on cubic and hexagonal lattices. Previous studies have revealed that both polymorphs of ZnIn_2S_4 are active for photocatalytic H_2 production under visible light irradiations and show considerable chemical stability [8–10]. However, the photocatalytic hydrogen production activity over pure ZnIn_2S_4 is low because of the poor separation efficiency and low migration ability of the photoexcited charge carriers. Sometimes an expensive Pt cocatalyst should be loaded onto ZnIn_2S_4 to enhance the

photocatalytic H_2 production activity of ZnIn_2S_4 [8–11]. For practical application, the photocatalytic performance of ZnIn_2S_4 should be further improved.

Metal-organic frameworks (MOFs) are a class of porous materials, which possess a three-dimensional (3D) crystal structure composed of metal units and organic ligands [12]. Owing to their high surface areas, well-defined porous structures and tunable pore sizes, MOFs are of great interest in terms of their potential applications in gas adsorption [13], separation [14], chemical sensing [15], drug delivery [16] and catalysis [17]. Recent progress has shown that some MOFs possess attractive semiconducting performance and can be used as photocatalyst. In fact, more and more photocatalysts based on MOFs applied in the degradation of organic pollutants [18], hydrogen production [19], CO_2 reduction [20] and organic transformations [21] have already been reported. Compared with traditional semiconductor photocatalysts, the MOF photocatalysts are beneficial because various combinations of metal-oxo clusters and bridging organic linkers allow for fine-tuning and rational design of these photocatalysts at the molecular level. Furthermore, intrinsic porosity of MOFs facilitates the diffusion of substrates and products through the open framework structures

* Corresponding author.

E-mail address: liuhong@shu.edu.cn (H. Liu).

<http://dx.doi.org/10.1016/j.apcatb.2017.09.043>

Received 30 June 2017; Received in revised form 12 August 2017; Accepted 18 September 2017

Available online 19 September 2017

0926-3373/ © 2017 Elsevier B.V. All rights reserved.

[22,23]. Despite the rapidly growing interest in MOFs, the MOF-based derivatives applied in photocatalysis are still in their early stage of exploration. Like all single component photocatalysts, MOFs, after light excitation, are subject to electron-hole recombination at significant rates. To improve the photocatalytic activities of MOFs, some strategies such as metal or ligand substitution [24,25] and noble metal deposition [26] have been employed. Besides, the formation of heterostructure by coupling MOFs with light-harvesting semiconductor materials is also a feasible route to promote the separation of photogenerated charge carriers and thus increase the photocatalytic activity. Recently, semiconductor@MOF heterostructures like ZnO@ZIF-8 [27], $\text{Cu}_3(\text{BTC})_2\text{@TiO}_2$ [28], $\text{BiVO}_4\text{@MIL-101}$ [29], $\text{Bi}_2\text{WO}_6\text{@UiO-66}$ [30], BiOBr@UiO-66 [31], $\text{UiO-66@g-C}_3\text{N}_4$ [32], CdS@UiO-66-NH_2 [23], $\text{MoS}_2\text{@UiO-66@CdS}$ [22] and $\text{Cd}_{0.2}\text{Zn}_{0.8}\text{S@UiO-66-NH}_2$ [33] have been synthesized and show great advantages due to their synergistic effect. However, to the best of our knowledge, no work related to $\text{ZnIn}_2\text{S}_4\text{@MOF}$ photocatalyst has been reported so far.

In this study, we report for the first time a new hybrid photocatalyst made by coupling amino-functionalized Ti-based MOF ($\text{NH}_2\text{-MIL-125(Ti)}$) and ZnIn_2S_4 . $\text{NH}_2\text{-MIL-125(Ti)}$ was selected as the representative MOF as it is relatively inexpensive, nontoxic, water-/photo-stable and visible-light responsive [34]. The as-prepared $\text{ZnIn}_2\text{S}_4\text{@NH}_2\text{-MIL-125(Ti)}$ nanocomposites showed a significantly enhanced photocatalytic performance for hydrogen production under visible-light ($\lambda > 420\text{ nm}$) irradiation. No noticeable decreases in the activity of the as prepared $\text{ZnIn}_2\text{S}_4\text{@NH}_2\text{-MIL-125(Ti)}$ photocatalysts were observed during the photocatalytic H_2 production. The possible mechanism for the excellent photocatalytic performance was also discussed.

2. Experimental

2.1. Materials

Indium chloride tetrahydrate ($\text{InCl}_3\cdot 4\text{H}_2\text{O}$), zinc chloride (ZnCl_2), thioacetamide (TAA), ethanol, methanol (MeOH), glycerol (GL), *N,N*-dimethylformamide (DMF) and tetrabutyl titanate $\text{Ti}(\text{OC}_4\text{H}_9)_4$ were provided by Sinopharm Chemical Reagent Company, Ltd. 2-Aminoterephthalic acid ($\text{NH}_2\text{-BDC}$) was purchased from J & K Scientific Co., Ltd. (Shanghai, China). All reagents were analytical grade and used without further purification.

2.2. Synthesis

2.2.1. Synthesis of $\text{NH}_2\text{-MIL-125(Ti)}$

In a typical synthesis, $\text{Ti}(\text{OC}_4\text{H}_9)_4$ (0.52 mL, 1.5 mmol) and $\text{NH}_2\text{-BDC}$ (1.087 g, 6.0 mmol) were added into a solution containing DMF (24.3 mL) and MeOH (2.7 mL). The above mixture was stirred for 30 min at room temperature, then was transferred to a Teflon-lined autoclave and maintained at 150°C for 24 h. The resulting mixture was cooled to room temperature and a yellow solid powder was recovered by centrifugation, washed with DMF and MeOH several times, and dried at 80°C .

2.2.2. Preparation of $\text{ZnIn}_2\text{S}_4\text{@NH}_2\text{-MIL-125(Ti)}$

The $\text{ZnIn}_2\text{S}_4\text{@NH}_2\text{-MIL-125(Ti)}$ nanocomposites were obtained by a one-step solvothermal method. In detail, a certain amount of as-prepared $\text{NH}_2\text{-MIL-125(Ti)}$ powder was dispersed into the mixture of DMF (15.0 mL) and GL (5.0 mL) with the aid of ultrasonication. Then, ZnCl_2 (0.136 g), $\text{InCl}_3\cdot 4\text{H}_2\text{O}$ (0.586 g) and TAA (0.301 g) was added into the mixture and stirred for 1 h at room temperature. Next, the obtained suspension was transferred into a 100 mL Teflon-lined stainless steel autoclave and maintained at 180°C for 10 h. After cooling to the room temperature, the resultant solid products were washed with distilled water and ethanol for several times and dried at 60°C . The as-synthesized $\text{ZnIn}_2\text{S}_4\text{@NH}_2\text{-MIL-125(Ti)}$ samples with 20 wt%, 30 wt%, 40 wt

% and 50 wt% $\text{NH}_2\text{-MIL-125(Ti)}$ were labeled as ZIS@NM20 , ZIS@NM30 , ZIS@NM40 and ZIS@NM50 , respectively. For comparison, the pure ZnIn_2S_4 was also synthesized by the same solvothermal process without addition of $\text{NH}_2\text{-MIL-125(Ti)}$.

2.3. Characterization

The crystal structure of the samples was identified by an X-ray diffractometer (XRD, D/MAX-2550, $\lambda = 0.15418\text{ nm}$) using $\text{Cu K}\alpha$ radiation. The morphologies and microstructures of the samples were analyzed by field-emission scanning electron microscopy (FE-SEM, JSM-6700F) equipped with an energy-dispersive X-ray spectrometry (EDS), transmission electron microscopy (TEM, JEOL 200CX) and high-resolution transmission electron microscopy (HRTEM, JEM-2010F). The high angle annular dark field scanning transmission electron microscopy (HAADF-STEM) and elemental mapping analysis were conducted by using a JEM-ARM 200F scanning transmission electron microscope. The X-ray photoelectron spectroscopy (XPS) measurement was carried out in a PHI ESCA-5000C electron spectrometer. UV-vis absorption spectra of the samples were recorded on a UV-vis spectrophotometer (Hitachi U-3010) with a wavelength range of 200–800 nm. Photoluminescence (PL) spectra were measured using a Hitachi F-7000 fluorescence spectrophotometer at room temperature. The Brunauer-Emmett-Teller (BET) specific surface areas of the samples were analyzed by nitrogen adsorption using a Micromeritics ASAP 2020 nitrogen adsorption apparatus.

2.4. Photocatalytic test

The photocatalytic H_2 production reactions were performed at room temperature in a 100 mL quartz reactor, which is connected to a closed-cycle circulation system. A 300 W Xenon lamp (PLS-SXE300C, Beijing Perfectlight Co. Ltd., China) equipped with a cut-off filter ($\lambda > 420\text{ nm}$) was used to provide the visible light irradiation. In a typical experiment, 50 mg photocatalyst was dispersed in a 100 mL aqueous solution containing 0.25 M Na_2SO_3 and 0.35 M Na_2S as sacrificial reagents. Before irradiation, the photo-reaction system was subjected to vacuum until the pressure gauge was stable. The reaction cell was kept at room temperature with cooling water. The produced H_2 was detected using an online gas chromatography (GC7900, N_2 carrier, 5A molecular sieve column, TCD detector).

The apparent quantum efficiency (AQE) for H_2 production was also measured under the same photocatalytic reaction conditions, only with a band-pass filter of 420 nm. The average intensity of irradiation was measured as 15.0 mW cm^{-2} (PL-MW2000 spectroradiometer) and the irradiation area was controlled at 28.26 cm^2 . The distance between the light source and the solution that produced hydrogen was 6.0 cm. The AQE was calculated according to following equation:

$$\text{AQE} = \frac{2 \times R_{\text{H}_2}}{I} \times 100\%$$

where R_{H_2} and I represent the H_2 production rate at 420 nm (molecules h^{-1}), and the rate of absorption of incident photons, respectively.

2.5. Photoelectrochemical measurements

The photocurrent measurements were carried out on a CHI-660 electrochemical workstation (Chenhua Instrument, Shanghai, China) in a conventional three electrode configuration with Pt foil as the counter electrode and an Ag/AgCl (saturated KCl) as the reference electrode. A 0.5 M Na_2SO_4 aqueous solution was used as the electrolyte. A 300 W Xe arc lamp served as a light source. The working electrodes were prepared as follows: 10 mg of the as-prepared photocatalyst was suspended in 1 mL ethanol to produce a slurry, which was then dip-coated onto an indium tin oxide (ITO) glass electrode. The coated area on the ITO glass was controlled to be 0.3 cm^2 . The film was dried in air and subsequently

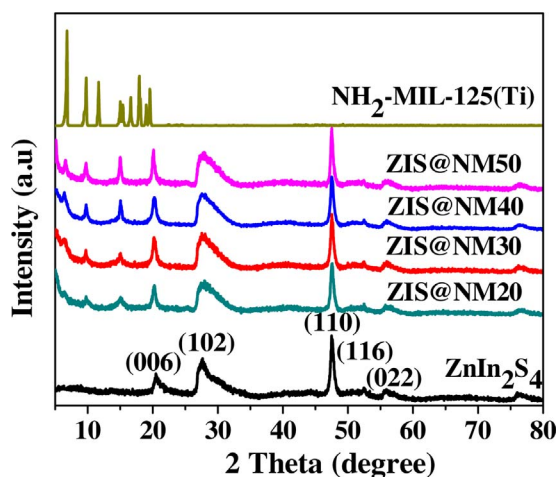


Fig. 1. The XRD patterns of $\text{NH}_2\text{-MIL-125(Ti)}$, ZnIn_2S_4 and $\text{ZnIn}_2\text{S}_4\text{@NH}_2\text{-MIL-125(Ti)}$ nanocomposites.

calcined at 120°C for 6 h. Electrochemical impedance spectroscopy (EIS) measurements were determined at an AC voltage magnitude of 5 mV with the frequency range of 10^6 to 0.01 Hz with the initial potential (0 V) in 0.01 M Na_2SO_4 . Mott-Schottky plots were carried out in the range of -0.5 to $+0.5$ V (vs. Ag/AgCl) reference electrode under frequency of 1 kHz and 2 kHz in 0.2 M Na_2SO_4 .

3. Results and discussion

3.1. Materials characterization

The phase structures of the as-obtained samples were determined by X-ray diffraction, as shown in Fig. 1. As can be seen, the pristine ZnIn_2S_4 shows diffraction peaks at $2\theta = 21.1^\circ$, 27.7° , 47.5° , 52.4° and 56.4° , which can be indexed to (006), (102), (110), (116) and (022) crystallographic planes of the hexagonal ZnIn_2S_4 (JCPDS No.65-2023) [10,35]. $\text{NH}_2\text{-MIL-125(Ti)}$ has the same diffraction peaks as reported in the literature [20,24,36]. For the $\text{ZnIn}_2\text{S}_4\text{@NH}_2\text{-MIL-125(Ti)}$ samples, besides the typical diffraction peaks of hexagonal phase ZnIn_2S_4 , three

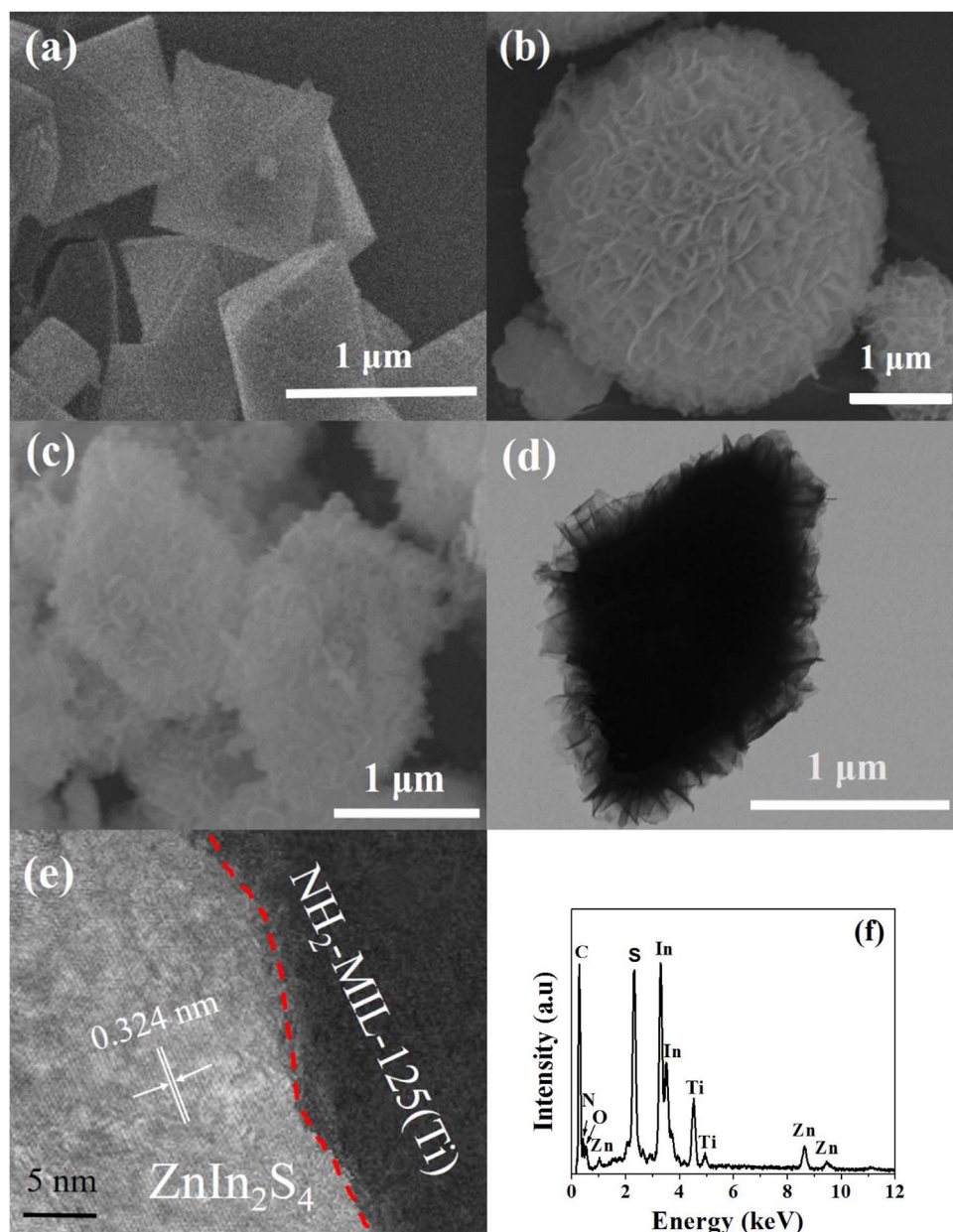


Fig. 2. SEM images of (a) $\text{NH}_2\text{-MIL-125(Ti)}$, (b) ZnIn_2S_4 , (c) ZIS@NM40 , (d) TEM, (e) HRTEM and (f) EDS spectrum of ZIS@NM40 .

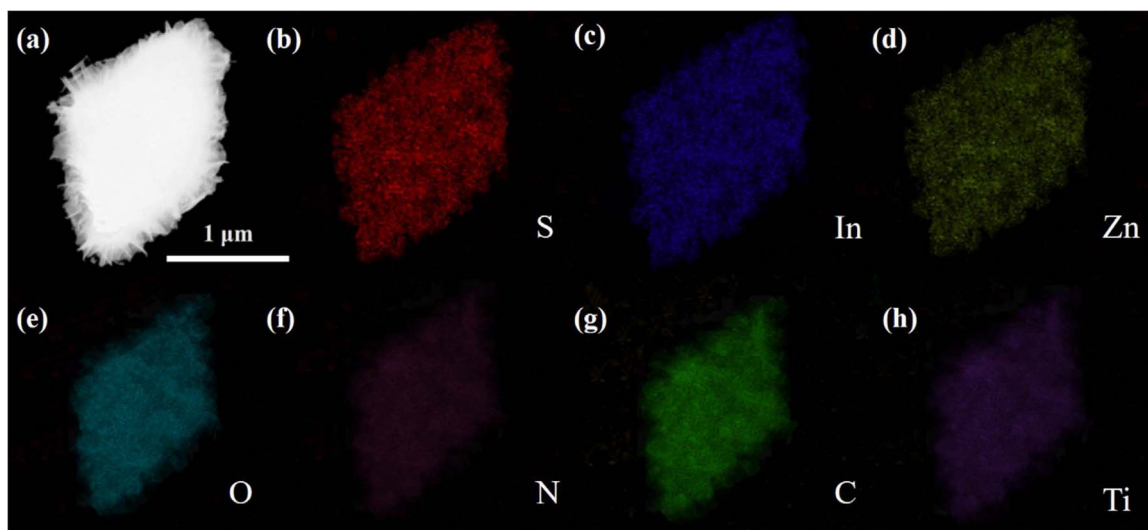


Fig. 3. (a) HAADF-STEM image and (b–h) elemental mapping images of ZIS@NM40.

additional peaks appear at 2θ value of 6.4° , 9.7° and 15.0° , which can be attributed to $\text{NH}_2\text{-MIL-125(Ti)}$. Furthermore, it can be observed that the peak intensities of the $\text{NH}_2\text{-MIL-125(Ti)}$ increase with increasing $\text{NH}_2\text{-MIL-125(Ti)}$ amount in the composites, which validates the co-existence of ZnIn_2S_4 and $\text{NH}_2\text{-MIL-125(Ti)}$ in the composites.

Fig. 2a–c present the SEM images of the pure $\text{NH}_2\text{-MIL-125(Ti)}$, ZnIn_2S_4 and the ZIS@NM40 sample, respectively. As shown in Fig. 2a, $\text{NH}_2\text{-MIL-125(Ti)}$ has octahedral shape with sharp edges and smooth surfaces. The average diameters of the octahedrons are approximately $1.0\ \mu\text{m}$. Pristine ZnIn_2S_4 (Fig. 2b) exhibits microsphere morphology, and the microsphere is composed of many cross-linked nanosheets. After hybridization with $\text{NH}_2\text{-MIL-125(Ti)}$, the ZnIn_2S_4 microspheres are unfolded and distributed uniformly as nanosheets on the surface of $\text{NH}_2\text{-MIL-125(Ti)}$ octahedrons (Fig. 2c). Fig. 2d shows the TEM image of ZIS@NM40. A two-layer composite structure is clearly observed. It can be seen that ZnIn_2S_4 nanosheets is as the outer layer attached on the surface of $\text{NH}_2\text{-MIL-125(Ti)}$, which is as the inlayer. The HRTEM image (Fig. 2e) of the heterostructures displays a clear lattice fringes with the nearest distance of $0.324\ \text{nm}$ coinciding with the value for the (102) plane of hexagonal ZnIn_2S_4 [8,10,37]. Additionally, the clear interface between $\text{NH}_2\text{-MIL-125(Ti)}$ and ZnIn_2S_4 is formed during ZnIn_2S_4 coating, which is very important for efficient charge transfer between $\text{NH}_2\text{-MIL-125(Ti)}$ and ZnIn_2S_4 . The EDS spectrum (Fig. 2f) confirms the presence of C, N, O, Zn, S, In and Ti elements in the composite.

The spatial distribution of different elements in the $\text{ZnIn}_2\text{S}_4\text{@NH}_2\text{-MIL-125(Ti)}$ composite were investigated by elemental mapping analysis (Fig. 3a–h). These images indicate that the O, N, C and Ti elements are distributed in the core of the composite, and the S, In and Zn elements are homogeneously distributed throughout the whole composite, further suggesting that the composite possesses a hierarchical core-shell structure with ZnIn_2S_4 as the shell around the $\text{NH}_2\text{-MIL-125(Ti)}$ core.

X-ray photoelectron spectroscopy (XPS) measurements were carried out to elucidate the surface composition and chemical states of the $\text{ZnIn}_2\text{S}_4\text{@NH}_2\text{-MIL-125(Ti)}$ composites. The survey XPS spectrum (Fig. 4a) of the ZIS@NM40 sample indicates that the composite mainly consists of C, N, O, Ti, S, In and Zn atoms, which is in good agreement with the EDS results. The C 1s spectrum shows four peak at $284.6\ \text{eV}$, $285.3\ \text{eV}$, $286.6\ \text{eV}$ and $288.8\ \text{eV}$ (Fig. 4b) corresponding to $\text{C}=\text{C}$, $\text{C}-\text{N}$, $\text{C}-\text{C}$, and $\text{C}=\text{O}$ of $\text{NH}_2\text{-BDC}$, respectively [38,39]. The peaks in the N 1s region (Fig. 4c) at $399.4\ \text{eV}$ and $402.3\ \text{eV}$ can be assigned to the N of the amine functionality stretching out or protruding into the cavities and the positively charged nitrogen ($-\text{N}=\text{N}^+$ and $-\text{NH}-\text{N}^+$) [38,39]. Fig. 4d shows Ti 2p spectrum of the ZIS@NM40 sample. The binding energy values of Ti $2p_{3/2}$ and Ti $2p_{1/2}$ at 458.8 and $464.5\ \text{eV}$,

respectively, indicate that titanium bounded to oxygen remains in oxidation state IV for the titanium-oxo cluster [38,39]. The O 1s spectrum (Fig. 4e) of ZIS@NM40 can be fitted into three peaks. The peak at $532.3\ \text{eV}$ is assigned to the OH group [38,39]. The peaks at 531.5 and $529.8\ \text{eV}$ can be ascribed to $\text{C}=\text{O}$ and titanium-oxo cluster, respectively [38,39]. The peaks centered at $1021.3\ \text{eV}$ and $1044.4\ \text{eV}$ (Fig. 4f) correspond to Zn $2p_{3/2}$ and Zn $2p_{1/2}$, respectively [35,37,40]. As for In 3d XPS spectrum (Fig. 4g), the peaks at $444.4\ \text{eV}$ and $451.2\ \text{eV}$ are assigned to In $3d_{5/2}$ and In $3d_{3/2}$, respectively [35,37,40]. The XPS spectrum of S 2p in Fig. 4h can be divided into two separated peaks centered at $161.2\ \text{eV}$ and $162.5\ \text{eV}$, which can be indexed to S $2p_{3/2}$ and S $2p_{1/2}$, respectively [35,37,40]. The XPS results demonstrate the co-existence of ZnIn_2S_4 and $\text{NH}_2\text{-MIL-125(Ti)}$ in the $\text{ZnIn}_2\text{S}_4\text{@NH}_2\text{-MIL-125(Ti)}$ composite.

The surface areas and porous structure of the samples were analyzed by N_2 adsorption-desorption experiment, and the results are shown in Fig. 5 and Table 1. N_2 adsorption-desorption isotherms of the $\text{NH}_2\text{-MIL-125(Ti)}$ sample exhibited a type I isotherm at $77\ \text{K}$ with no hysteresis, indicating its typical microporous structure [33,38]. The ZnIn_2S_4 have type IV isotherm with a discrete hysteresis loop (H3 type) in the higher relative pressure (P/P_0 , $0.47\text{--}1.0$) range, which implies the presence of slit-like pores and capillary condensation in the mesoporous [33,41]. All $\text{ZnIn}_2\text{S}_4\text{@NH}_2\text{-MIL-125(Ti)}$ samples exhibit hybrid type I/IV isotherms with large hysteresis between adsorption and desorption branches, confirming the presence of both of micropores and mesopores. The surface area and pore volume of ZnIn_2S_4 are $98.6\ \text{m}^2\ \text{g}^{-1}$ and $0.0896\ \text{cm}^3\ \text{g}^{-1}$, respectively. For $\text{NH}_2\text{-MIL-125(Ti)}$, the corresponding values are $1338.0\ \text{m}^2\ \text{g}^{-1}$ and $0.5830\ \text{cm}^3\ \text{g}^{-1}$. After incorporating $\text{NH}_2\text{-MIL-125(Ti)}$, the surface area and pore volume of $\text{ZnIn}_2\text{S}_4\text{@NH}_2\text{-MIL-125(Ti)}$ increase drastically with increasing $\text{NH}_2\text{-MIL-125(Ti)}$ content (Table 1). It is suggested that the hierarchical structure with a higher surface area can offer more catalytically active sites for the adsorption of a large amount of substrate.

The optical absorption characteristics of pristine $\text{NH}_2\text{-MIL-125(Ti)}$, ZnIn_2S_4 , and the composite materials with different weight percentages of $\text{NH}_2\text{-MIL-125(Ti)}$ were measured by the UV–vis diffuse reflectance spectroscopy (Fig. 6a). Pristine $\text{NH}_2\text{-MIL-125(Ti)}$ possesses two absorption edges at around $325\ \text{nm}$ and $525\ \text{nm}$, corresponding to the absorption of Ti–O oxo-clusters and the ligand-based absorption, respectively [20,24]. The absorption edge of pure ZnIn_2S_4 is determined to be $600\ \text{nm}$, which can be assigned to intrinsic band gap absorption. The $\text{ZnIn}_2\text{S}_4\text{@NH}_2\text{-MIL-125(Ti)}$ composites have absorption edges of longer wavelengths in comparison with the pristine $\text{NH}_2\text{-MIL-125(Ti)}$. The red shift might suggest that the composites can absorb more visible

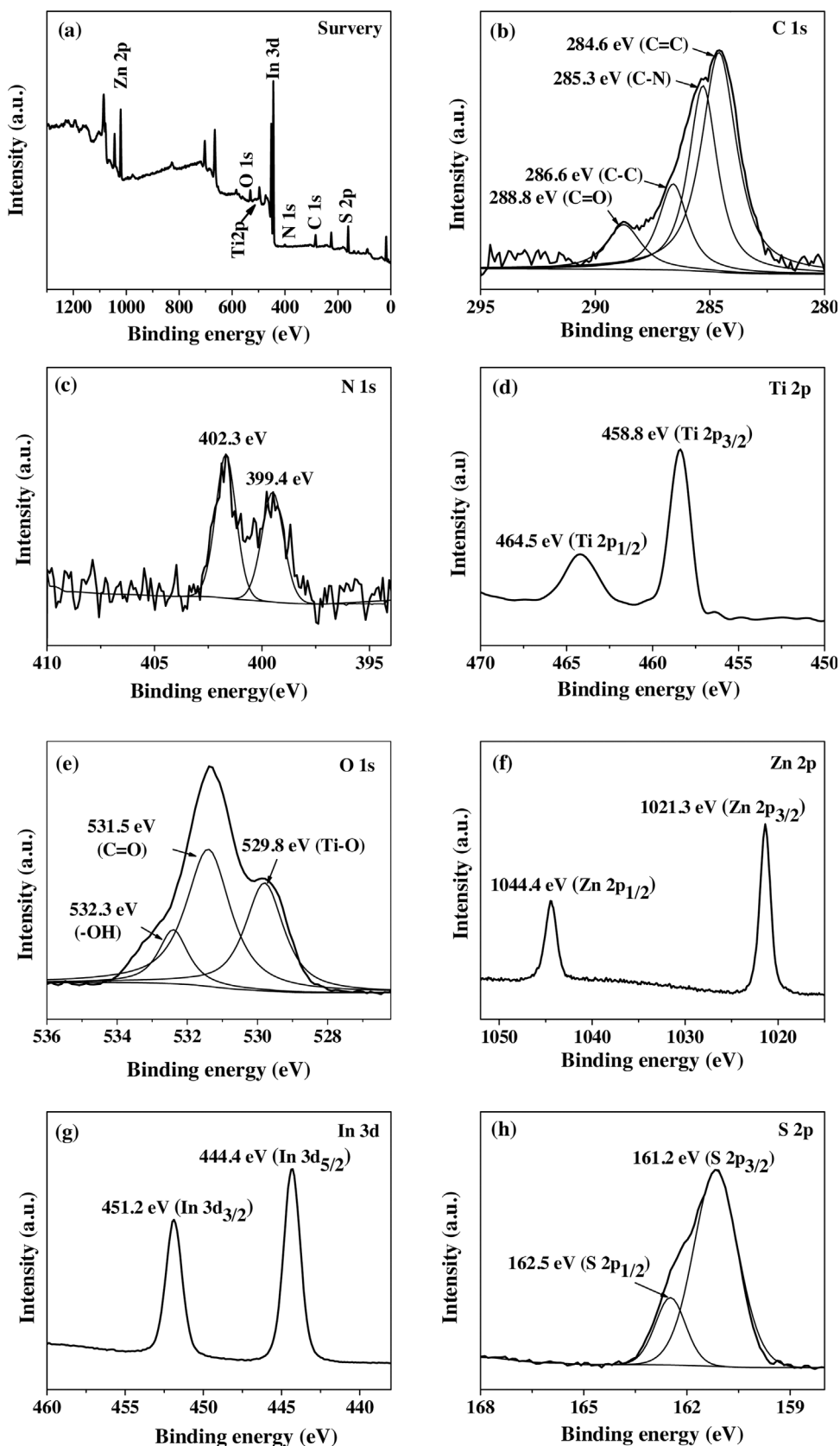


Fig. 4. XPS spectra of ZIS@NM40: (a) survey, (b) C 1s, (c) N 1s, (d) Ti 2p, (e) O 1s, (f) Zn 2p, (g) In 3d, (h) S 2p.

light, which may result in generation of more electron-hole pairs. The band gap energies (E_g) of the samples can be obtained from plots of $(\alpha h\nu)^2$ versus photon energy ($h\nu$) [37,38]. As shown in Fig. 6b, the E_g values of ZnIn_2S_4 , ZIS@NM20, ZIS@NM30, ZIS@NM40, ZIS@NM50

and $\text{NH}_2\text{-MIL-125(Ti)}$ are estimated to be 2.40, 2.44, 2.48, 2.55, 2.59 and 2.74 eV, respectively.

The valence band (VB) edge potential (E_{VB}) of ZnIn_2S_4 can be determined using the following equation: $E_{VB} = X - E^e + 0.5E_g$, where X

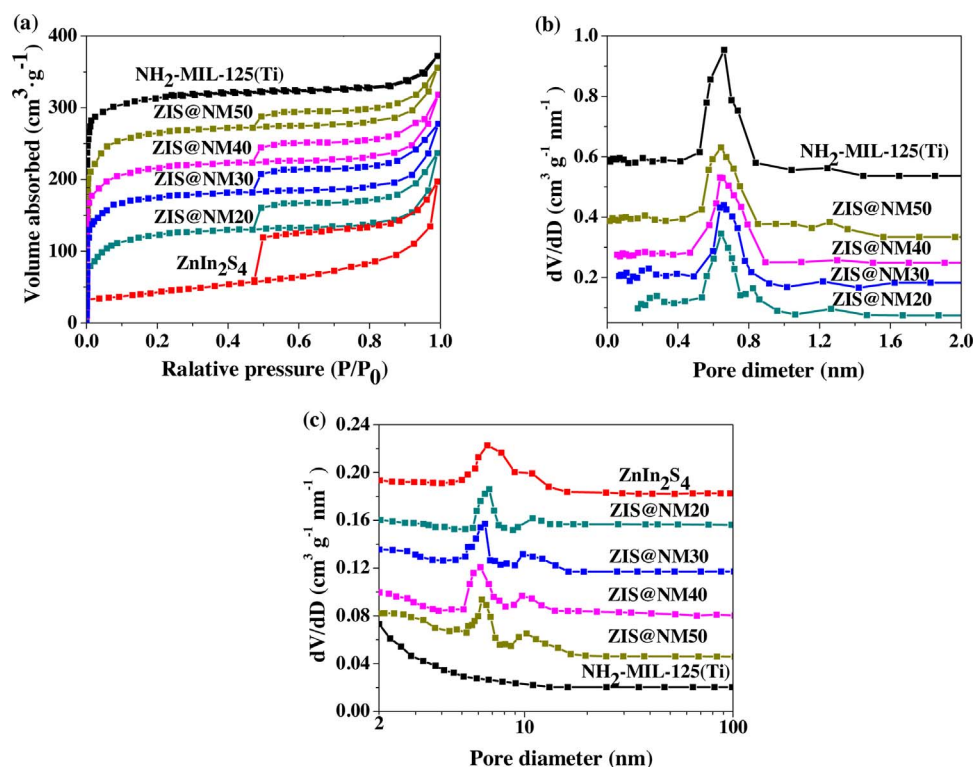


Fig. 5. (a) Nitrogen adsorption-desorption isotherms, (b) Horvath-Kawazoe (HK) micropore size distributions and (c) Barrett-Joyner-Halenda (BJH) mesopore size distributions of as-prepared sample.

Table 1
Summary of textural properties and photocatalytic activities of the samples.

Samples	S_{BET} ($\text{m}^2 \cdot \text{g}^{-1}$)	Pore volume ($\text{cm}^3 \cdot \text{g}^{-1}$)	Average pore size (nm)	H_2 production rate ($\mu\text{mol} \cdot \text{h}^{-1} \cdot \text{g}^{-1}$)	Normalized H_2 production rate ($\mu\text{mol} \cdot \text{h}^{-1} \cdot \text{m}^{-2}$)	AQE (%)
ZnIn_2S_4	98.6	0.0896	9.26	339.1	3.439	1.1
ZIS@NM20	288.5	0.2348	5.72	1069.9	3.708	1.9
ZIS@NM30	459.3	0.3104	4.24	1705.6	3.713	3.0
ZIS@NM40	521.8	0.3672	3.56	2204.2	4.224	4.3
ZIS@NM50	672.2	0.4112	2.92	1125.6	1.674	2.4
$\text{NH}_2\text{-MIL-125(Ti)}$	1338.0	0.5830	0.66	0	0	0

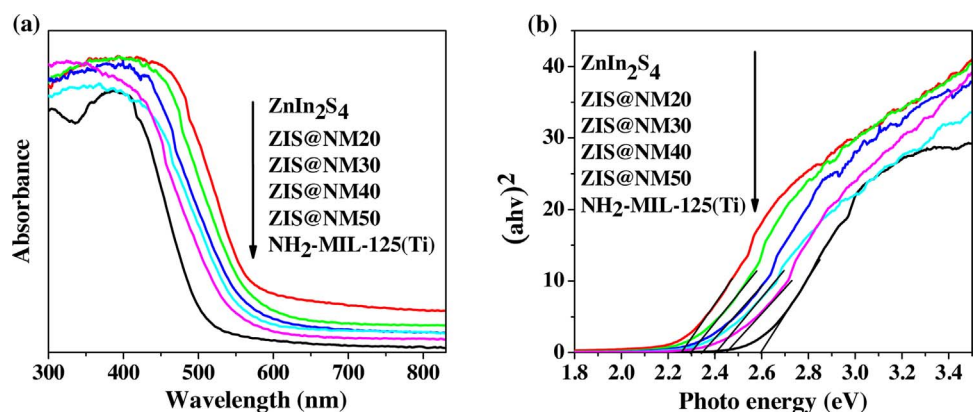


Fig. 6. (a) UV-vis diffuse reflectance absorption spectra of $\text{NH}_2\text{-MIL-125(Ti)}$, ZnIn_2S_4 , $\text{ZnIn}_2\text{S}_4/\text{NH}_2\text{-MIL-125(Ti)}$ composites, and (b) plots of $(\alpha h\nu)^2$ against photon energy.

is the electronegativity of the semiconductor estimated by the geometric mean of the electronegativity of the constituent atoms. E^e is the energy of free electrons on the hydrogen scale (~ 4.5 eV). The conduction band (CB) edge potential (E_{CB}) can be determined by $E_{\text{CB}} = E_{\text{VB}} - E_g$. The X value of pure ZnIn_2S_4 is about 4.86 eV. The E_{VB} of bare ZnIn_2S_4 can be assigned to be +1.56 eV, and the corresponding E_{CB} of ZnIn_2S_4 can be estimated to be -0.84 eV. Fig. 7 shows a typical Mott-Schottky plot of $\text{NH}_2\text{-MIL-125(Ti)}$ measured at a frequency of 1000 and 2000 Hz, which reveals the typical n -type characteristics for

$\text{NH}_2\text{-MIL-125(Ti)}$. The flat band potential of $\text{NH}_2\text{-MIL-125(Ti)}$ derived from Mott-Schottky plot is about -0.82 V vs. Ag/AgCl (i.e. -0.62 V vs. NHE). Since it is generally believed that the bottom of the conduction band in many n -type semiconductors is more negative by about 0.10 V than the flat band potential [42,43], the conduction band (LUMO) of $\text{NH}_2\text{-MIL-125(Ti)}$ can be estimated to be -0.72 V vs. NHE. Combination of the bandgap value of $\text{NH}_2\text{-MIL-125(Ti)}$ obtained by DRS analysis (Fig. 6), the valence band (HOMO) can be calculated to be +2.02 V vs. NHE.

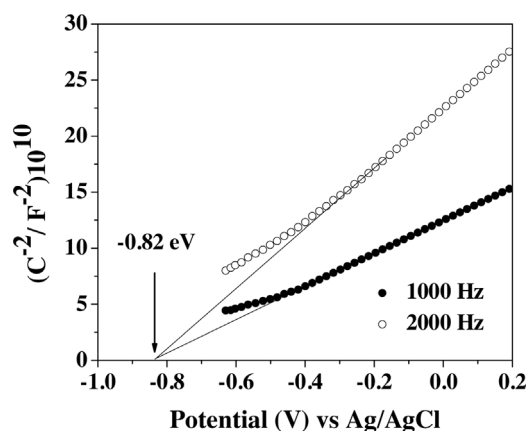


Fig. 7. Mott-Schottky plot of $\text{NH}_2\text{-MIL-125(Ti)}$ in a 0.2 M Na_2SO_4 aqueous solution (pH = 6.8).

3.2. Photocatalytic H_2 production activity

The photocatalytic hydrogen production activities of the as-prepared samples were evaluated under visible light irradiation ($\lambda > 420 \text{ nm}$) using Na_2S and Na_2SO_3 as sacrificial agents. As shown in Fig. 8 and Table 1, when $\text{NH}_2\text{-MIL-125(Ti)}$ alone is used as the photocatalyst, no H_2 is detected, suggesting $\text{NH}_2\text{-MIL-125(Ti)}$ itself is inactive to photocatalytic hydrogen production. Meanwhile, pristine ZnIn_2S_4 exhibits a very low photocatalytic activity with the H_2 production rate of $339.1 \mu\text{mol}\cdot\text{h}^{-1}\cdot\text{g}^{-1}$. After coupling with $\text{NH}_2\text{-MIL-125(Ti)}$, the photocatalytic activity of ZnIn_2S_4 is significantly enhanced. The rate of H_2 production over $\text{ZnIn}_2\text{S}_4@\text{NH}_2\text{-MIL-125(Ti)}$ composites increases with increasing $\text{NH}_2\text{-MIL-125(Ti)}$ content, achieving a maximum of $2204.2 \mu\text{mol}\cdot\text{h}^{-1}\cdot\text{g}^{-1}$ (with a 4.3% apparent quantum efficiency at 420 nm) at the $\text{NH}_2\text{-MIL-125(Ti)}$ content of 40 wt%, which is about 6.5 times higher than that of pure ZnIn_2S_4 . However, a further increase in the content of $\text{NH}_2\text{-MIL-125(Ti)}$ leads to a decrease in the photocatalytic H_2 production. This decrease is probably due to the following factors: (i) accompanying with the increase of $\text{NH}_2\text{-MIL-125(Ti)}$, the content of ZnIn_2S_4 , which is the only activity phase, will be decreased relatively. (ii) overmuch $\text{NH}_2\text{-MIL-125(Ti)}$ may turn into a recombination center of photoinduced charges (this can be confirmed by the photoluminescence measurement as shown in Fig. 10a), which will cause reduction of activity. Therefore, an appropriate $\text{NH}_2\text{-MIL-125(Ti)}$ amount is important to achieve the optimal H_2 production rate of $\text{ZnIn}_2\text{S}_4@\text{NH}_2\text{-MIL-125(Ti)}$ hybrids. Considering the difference in surface area of the as-prepared samples, we also normalized the H_2 production rates with respect to the surface areas of the materials (Table 1). It is found that the order of the normalized rates is nearly same as the original order and the ZIS@NM40 sample still shows the best performance. Notably, the photocatalytic H_2 production activity of

the ZIS@NM40 sample is also higher than the various ZnIn_2S_4 -based photocatalysts reported previously, such as reduced graphene oxide (RGO)/ ZnIn_2S_4 [44], $\text{In}_2\text{S}_3/\text{ZnIn}_2\text{S}_4$ [45], Pt/carbon quantum dots- ZnIn_2S_4 [46], $\text{MoS}_2/\text{ZnIn}_2\text{S}_4$ [47], g- C_3N_4 /nanocarbon/ ZnIn_2S_4 [48], ZnIn_2S_4 /RGO/ MoS_2 [49], La- ZnIn_2S_4 [50], O-doped ZnIn_2S_4 [51], CuS/ $\text{CdIn}_2\text{S}_4/\text{ZnIn}_2\text{S}_4$ [52], $\text{ZnIn}_2\text{S}_4/\text{In(OH)}_3$ [53], and so on.

In addition to the high H_2 production activity, the good reusability is another key factor for highly efficient photocatalyst. In order to determine the stability of photocatalyst, the time courses of visible-light-driven H_2 production over ZIS@NM40 was evaluated. As shown in Fig. 9a, the H_2 production activity of the ZIS@NM40 photocatalyst did not drop obviously after five recycles, indicating the ZIS@NM40 photocatalyst have a good stability. Moreover, according to the XRD results shown in Fig. 9b, it was found that ZIS@NM40 still preserved its original integrity well after photocatalytic cycles. The SEM observation (Fig. 9c) also show that the morphology of ZIS@NM40 after the photocatalytic reaction kept well. The above results indicate that the stability of ZIS@NM40 is satisfying, which is important for its further practical applications.

3.3. Mechanism of the enhancement of photocatalytic activity

It is known that the photocatalytic activity of a semiconductor photocatalyst is dependent on the trapping and lifetime of photo-generated charges. The photoluminescence (PL) emission spectrum is often employed to study the surface structure and excited states, and it can provide useful information about charge carrier trapping and recombination in a semiconductor since the PL emission comes from the recombination of free charge carriers [33,41]. Fig. 10a shows a comparison among the PL emission spectra of the different samples monitored at an excitation wavelength of 385 nm. It can be seen pure ZnIn_2S_4 shows a strong emission peak at around 445 nm. For the $\text{ZnIn}_2\text{S}_4@\text{NH}_2\text{-MIL-125(Ti)}$ composites, their PL spectra are similar to that of pure ZnIn_2S_4 , but a significant fluorescence peak decrease is observed. Such an apparent decrease of fluorescence peak intensity indicates the low recombination rate of photogenerated electrons and holes in $\text{ZnIn}_2\text{S}_4@\text{NH}_2\text{-MIL-125(Ti)}$ system. Moreover, the order of PL intensity is $\text{ZnIn}_2\text{S}_4 > \text{ZIS@NM20} > \text{ZIS@NM50} > \text{ZIS@NM30} > \text{ZIS@NM40}$, which agrees well with the observed results of their photocatalytic activity mentioned above. The interface charge separation efficiency can be further investigated by the photoelectrochemical technique. Fig. 10b shows the transient photocurrent response of pure $\text{NH}_2\text{-MIL-125(Ti)}$, ZnIn_2S_4 and ZIS@NM40 under visible light irradiation for several on-off cycles. The pure $\text{NH}_2\text{-MIL-125(Ti)}$ sample shows a very low photocurrent density, which can be attributed to the fast recombination of photogenerated electrons and holes in $\text{NH}_2\text{-MIL-125(Ti)}$. The unmodified ZnIn_2S_4 photoelectrode generated anodic photocurrent with a value of $0.54 \mu\text{A}\cdot\text{cm}^{-2}$. The $\text{ZnIn}_2\text{S}_4@\text{NH}_2\text{-MIL-125(Ti)}$ composite (ZIS@NM40) shows higher photocurrent intensity

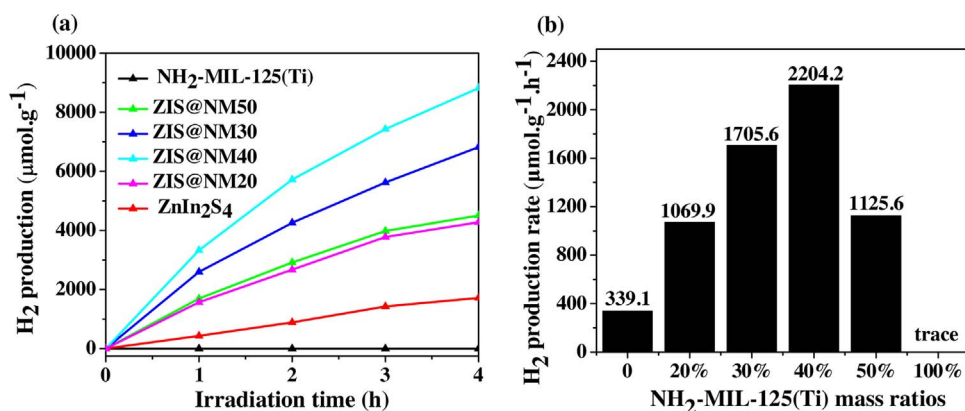


Fig. 8. (a) Plots of photocatalytic H_2 production amount vs. irradiation time and (b) comparison of the visible-light induced H_2 production rate for as-synthesized samples.

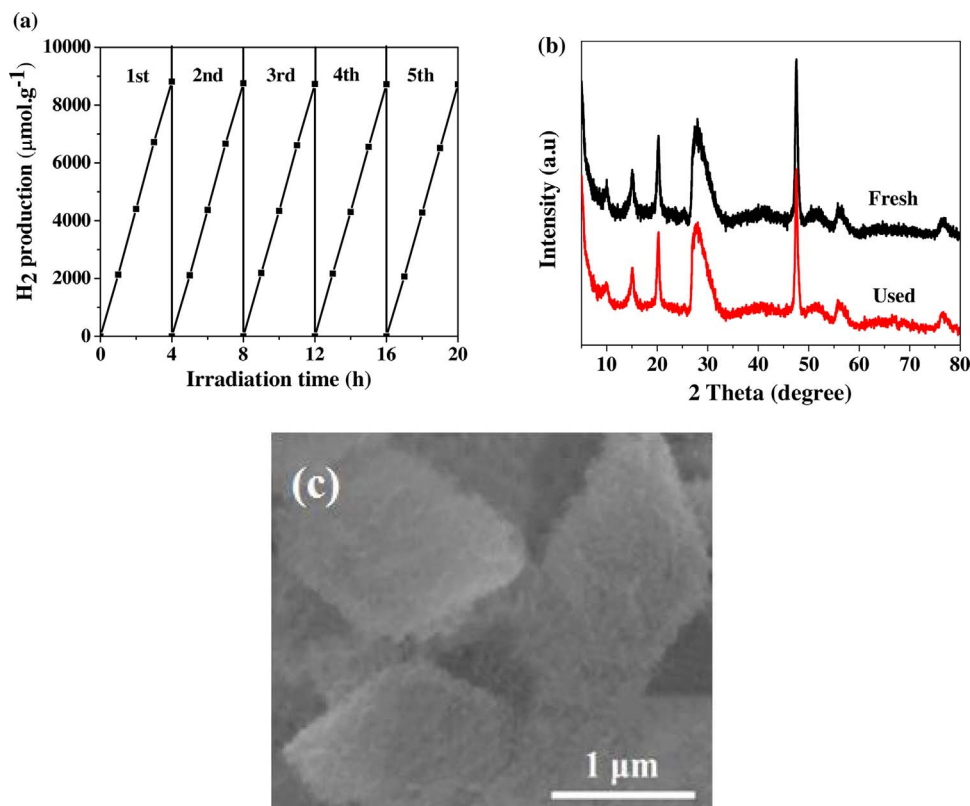


Fig. 9. (a) Cycling test of photocatalytic H₂ production activity over ZIS@NM40, (b) XRD patterns of the fresh and used ZIS@NM40 and (c) SEM image of ZIS@NM40 after five cycles.

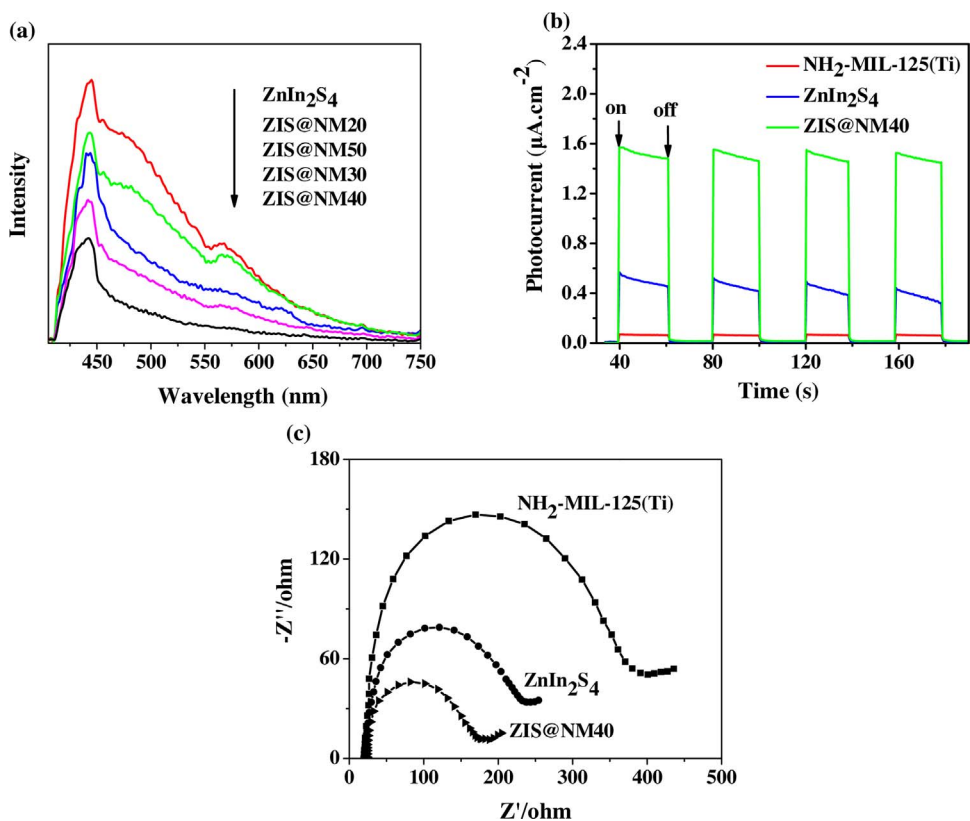


Fig. 10. (a) PL spectra, (b) transient photocurrent responses and (c) EIS Nyquist plots of the as-synthesized samples.

(1.57 μA.cm⁻²) than that of ZnIn₂S₄ and NH₂-MIL-125(Ti). These results indicate that the hybrid composite holds stronger ability in generating and transferring the photoexcited charge carrier under light irradiation. To further confirm the above results, electrochemical

impedance spectroscopy (EIS), a useful measurement to characterize charge carrier transportation, was also performed. As can be seen from Fig. 10c, the diameter of the Nyquist semicircle for the ZnIn₂S₄@NH₂-MIL-125(Ti) composite is smaller than that of ZnIn₂S₄ and NH₂-MIL-

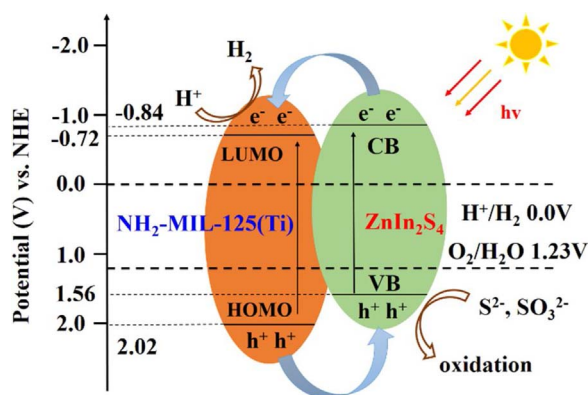


Fig. 11. Proposed charge transfer mechanism of the $\text{ZnIn}_2\text{S}_4@\text{NH}_2\text{-MIL-125(Ti)}$ composite.

125(Ti), which indicates that the hybrid composite has a lower resistance than that of ZnIn_2S_4 and $\text{NH}_2\text{-MIL-125(Ti)}$. Therefore, it can be concluded that the efficient transfer of photoinduced electrons between ZnIn_2S_4 and $\text{NH}_2\text{-MIL-125(Ti)}$ facilitates the electron-hole separation, and then improves the corresponding photocatalytic activity in H_2 production.

Based on above-mentioned results, the tentative mechanism proposed for the superior photocatalytic activity of $\text{ZnIn}_2\text{S}_4@\text{NH}_2\text{-MIL-125(Ti)}$ photocatalyst is illustrated in Fig. 11. Under the visible light illumination, both ZnIn_2S_4 and $\text{NH}_2\text{-MIL-125(Ti)}$ can be excited and engender photogenerated electron-hole pairs. The CB of ZnIn_2S_4 (-0.84 eV) is more negative than that of $\text{NH}_2\text{-MIL-125(Ti)}$ (-0.72 eV), and the HOMO of $\text{NH}_2\text{-MIL-125(Ti)}$ ($+2.02$ eV) is more positive than that of ZnIn_2S_4 ($+1.56$ eV). Considering the inner electric field and energy band structure of the heterojunction, the photoexcited electrons on the CB of ZnIn_2S_4 can rapidly transfer to the LUMO of $\text{NH}_2\text{-MIL-125(Ti)}$, while the photogenerated holes on the HOMO of $\text{NH}_2\text{-MIL-125(Ti)}$ can migrate to the VB of ZnIn_2S_4 . As a result, the photogenerated electron-hole pairs can be separated efficiently in the photocatalytic system of $\text{ZnIn}_2\text{S}_4@\text{NH}_2\text{-MIL-125(Ti)}$, leading to a significantly enhanced photocatalytic H_2 production activity than the pure ZnIn_2S_4 .

4. Conclusions

A series of heterostructured $\text{ZnIn}_2\text{S}_4@\text{NH}_2\text{-MIL-125(Ti)}$ nanocomposites with different $\text{NH}_2\text{-MIL-125(Ti)}$ contents were fabricated via a facile solvothermal method. The prepared $\text{ZnIn}_2\text{S}_4@\text{NH}_2\text{-MIL-125(Ti)}$ composites showed high photocatalytic activity for H_2 production under visible light irradiation. The optimal $\text{NH}_2\text{-MIL-125(Ti)}$ content was determined to be 40 wt% and the corresponding H_2 production rate was $2204.2 \mu\text{mol h}^{-1} \text{g}^{-1}$, which was nearly 6.5 times higher than that of pure ZnIn_2S_4 . In addition, the resultant $\text{ZnIn}_2\text{S}_4@\text{NH}_2\text{-MIL-125(Ti)}$ composites also exhibited good stability and recycling performance. This work not only highlights the intrinsic role of MOFs materials in the enhanced photocatalytic performance of ZnIn_2S_4 semiconductor for H_2 production, but also provides significant guidance to take full advantage of predominant properties of MOFs in designing more efficient photocatalysts.

Acknowledgments

The authors gratefully acknowledge the National Natural Science Foundation of China (11472164) and Innovative Research Team (IRT13078) for financial support. The authors also thank Lab for Microstructure, Instrumental Analysis and Research Center, Shanghai University, for materials characterizations.

References

- [1] Y. Noda, B. Lee, K. Domen, J.N. Kondo, Synthesis of crystallized mesoporous tantalum oxide and its photocatalytic activity for overall water splitting under ultraviolet light irradiation, *Chem. Mater.* 20 (2008) 5361–5367.
- [2] B. Seger, T. Pedersen, A.B. Laursen, P.C.K. Vesborg, O. Hansen, I. Chorkendorff, Using TiO_2 as a conductive protective layer for photocathodic H_2 evolution, *J. Am. Chem. Soc.* 135 (2013) 1057–1064.
- [3] K. Zhang, L.J. Guo, Metal sulphide semiconductors for photocatalytic hydrogen production, *Catal. Sci. Technol.* 3 (2013) 1672–1690.
- [4] K. Ikeue, S. Shiiba, M. Machida, Novel visible-light-driven photocatalyst based on Mn-Cd-S for efficient H_2 evolution, *Chem. Mater.* 22 (2010) 743–745.
- [5] K. Maeda, K. Domen, Solid solution of GaN and ZnO as a stable photocatalyst for overall water splitting under visible light, *Chem. Mater.* 22 (2010) 612–623.
- [6] X.C. Wang, K. Maeda, A. Thomas, K. Takanabe, G. Xin, J.M. Carlsson, K. Domen, M. Antonietti, A metal-free polymeric photocatalyst for hydrogen production from water under visible light, *Nature Mater.* 8 (2009) 76–80.
- [7] Z.W. Zhao, Y.J. Sun, F. Dong, Graphitic carbon nitride based nanocomposites: a review, *Nanoscale* 7 (2015) 15–37.
- [8] B. Chai, T.Y. Peng, P. Zeng, X.H. Zhang, X.J. Liu, Template-free hydrothermal synthesis of ZnIn_2S_4 flowered microspheres as an efficient photocatalyst for H_2 production under visible-light irradiation, *J. Phys. Chem. C* 115 (2011) 6149–6155.
- [9] J. Shen, J.T. Zai, Y.P. Yuan, X.F. Qian, 3D hierarchical ZnIn_2S_4 : The preparation and photocatalytic properties on water splitting, *Int. J. Hydrogen Energy* 37 (2012) 16986–16993.
- [10] L. Shang, C. Zhou, T. Bian, H.J. Yu, L.Z. Wu, C.H. Tung, T.R. Zhang, Facile synthesis of hierarchical ZnIn_2S_4 submicrospheres composed of ultrathin mesoporous nanosheets as a highly efficient visible-light-driven photocatalyst for H_2 production, *J. Mater. Chem. A* 1 (2013) 4552–4558.
- [11] F. Tian, R.S. Zhu, K.L. Song, M.L. Niu, F. Ouyang, G. Cao, The effects of hydrothermal temperature on the photocatalytic performance of ZnIn_2S_4 for hydrogen generation under visible light irradiation, *Mater. Res. Bull.* 70 (2015) 645–650.
- [12] V. Guillermin, D. Kim, J.F. Eubank, R. Luebke, X. Liu, K. Adil, M.S. Lah, M. Eddaoudi, A supermolecular building approach for the design and construction of metal-organic frameworks, *Chem. Soc. Rev.* 43 (2014) 6141–6172.
- [13] M. Eddaoudi, J. Kim, N. Rosi, D. Vodak, J. Wachter, M. O’Keeffe, O.M. Yaghi, Systematic design of pore size and functionality in isoreticular MOFs and their application in methane storage, *Science* 295 (2002) 469–472.
- [14] Z.X. Zhao, X.L. Ma, A. Kasik, Z. Li, Y.S. Lin, Gas separation properties of thin metal organic framework (MOF-5) Membranes, *Ind. Eng. Chem. Res.* 52 (2013) 1102–1108.
- [15] I. Stassen, N. Burtch, A. Talin, P. Falcaro, M. Allendorf, R. Ameloot, An updated roadmap for the integration of metal-organic frameworks with electronic devices and chemical sensors, *Chem. Soc. Rev.* 46 (2017) 3185–3241.
- [16] W. Cai, C.C. Chu, G. Liu, Y.J. Wang, Metal-organic framework-based nanomedicine platforms for drug delivery and molecular imaging, *Small* 37 (2015) 4806–4822.
- [17] D. Farrusseng, S. Aguado, C. Pinel, Metal-organic frameworks: opportunities for catalysis, *Angew. Chem. Int. Ed.* 48 (2009) 7502–7513.
- [18] C.H. Zhang, L.H. Ai, J. Jiang, Solvothermal synthesis of MIL-53(Fe) hybrid magnetic composites for photoelectrochemical water oxidation and organic pollutant photodegradation under visible light, *J. Mater. Chem. A* 3 (2015) 3074–3081.
- [19] P.Y. Wu, M. Jiang, Y. Li, Y.H. Liu, J. Wang, Highly efficient photocatalytic hydrogen production from pure water via a photoactive metal-organic framework and its PDMS@MOF, *J. Mater. Chem. A* 5 (2017) 7833–7838.
- [20] Y.H. Fu, D.R. Sun, Y.J. Chen, R.K. Huang, Z.X. Ding, X.Z. Fu, Z.H. Li, An amine-functionalized titanium metal-organic framework photocatalyst with visible-light-induced activity for CO_2 reduction, *Angew. Chem. Int. Ed.* 51 (2012) 3364–3367.
- [21] D.K. Wang, M.T. Wang, Z.H. Li, Fe-based metal-organic frameworks for highly selective photocatalytic benzene hydroxylation to phenol, *ACS Catal.* 5 (2015) 6852–6857.
- [22] L.J. Shen, M.B. Luo, Y.H. Liu, R.W. Liang, F.F. Jing, L. Wu, Noble-metal-free MoS_2 co-catalyst decorated UiO-66/CdS hybrids for efficient photocatalytic H_2 production, *Appl. Catal. B: Environ.* 166–167 (2015) 445–453.
- [23] L.J. Shen, S.J. Liang, W.M. Wu, R.W. Liang, L. Wu, CdS-decorated $\text{UiO-66(NH}_2\text{)}$ nanocomposites fabricated by a facile photodeposition process: an efficient and stable visible-light-driven photocatalyst for selective oxidation of alcohols, *J. Mater. Chem. A* 1 (2013) 11473–11482.
- [24] Y.H. Fu, L. Sun, H. Yang, L. Xu, F.M. Zhang, W.D. Zhu, Visible-light-induced aerobic photocatalytic oxidation of aromatic alcohols to aldehydes over Ni-doped $\text{NH}_2\text{-MIL-125(Ti)}$, *Appl. Catal. B: Environ.* 187 (2016) 212–217.
- [25] L.J. Shen, R.W. Liang, M.B. Luo, F.F. Jing, L. Wu, Electronic effects of ligand substitution on metal-organic framework photocatalysts: the case study of UiO-66 , *Phys. Chem. Chem. Phys.* 17 (2015) 117–121.
- [26] C. Wang, K.E. deKrafft, W.B. Lin, Pt nanoparticles@photoactive metal-organic frameworks: efficient hydrogen evolution via synergistic photoexcitation and electron injection, *J. Am. Chem. Soc.* 134 (2012) 7211–7214.
- [27] X.B. Wang, J. Liu, S. Leong, X.C. Lin, J. Wei, B. Kong, Y.F. Xu, Z.X. Low, J.F. Yao, H.T. Wang, Rapid construction of ZnO@ZIF-8 heterostructures with size-selective photocatalysis properties, *ACS Appl. Mater. Inter.* 8 (2016) 9080–9087.
- [28] R. Li, J.H. Hu, M.S. Deng, H.L. Wang, X.J. Wang, Y.L. Hu, H.L. Jiang, J. Jiang, Q. Zhang, Y. Xie, Y.J. Xiong, Integration of an inorganic semiconductor with a metal-organic framework: a platform for enhanced gaseous photocatalytic reactions, *Adv. Mater.* 26 (2014) 4783–4788.
- [29] Y.L. Xu, M.M. Lv, H.B. Yang, Q. Chen, X.T. Liu, F.Y. Wei, $\text{BiVO}_4/\text{MIL-101}$ composite having the synergistically enhanced visible light photocatalytic activity, *RSC Adv.* 5

- (2015) 43473–43479.
- [30] Z. Sha, J.L. Sun, H.S.O. Chan, S. Jaenicke, J.S. Wu, Bismuth tungstate incorporated zirconium metal organic framework composite with enhanced visible- light photocatalytic performance, *RSC Adv.* 4 (2014) 64977–64984.
 - [31] Z. Sha, J.S. Wu, Enhanced visible-light photocatalytic performance of BiOBr/Uio-66(Zr) composite for dye degradation with the assistance of Uio-66, *RSC Adv.* 5 (2015) 39592–39600.
 - [32] R. Wang, L.N. Gu, J.J. Zhou, X.L. Liu, F. Teng, C.H. Li, Y.H. Shen, Y.P. Yuan, Quasi-polymeric metal-organic framework Uio-66/g-C₃N₄ heterojunctions for enhanced photocatalytic hydrogen evolution under visible light irradiation, *Adv. Mater. Interfaces* 2 (2015) 1500037.
 - [33] Y. Su, Z. Zhang, H. Liu, Y. Wang, Cd_{0.2}Zn_{0.8}S@Uio-66-NH₂ nanocomposites as efficient and stable visible-light-driven photocatalyst for H₂ evolution and CO₂ reduction, *Appl. Catal. B-Environ.* 200 (2017) 448–457.
 - [34] H. Wang, X.Z. Yuan, Y. Wu, X.H. Chen, L.J. Leng, G.M. Zeng, Photodeposition of metal sulfides on titanium metal-organic frameworks for excellent visible-light-driven photocatalytic Cr(VI) reduction, *RSC Adv.* 5 (2015) 32531–32535.
 - [35] L. Ye, Z.H. Li, Rapid microwave-assisted syntheses of reduced graphene oxide (RGO)/ZnIn₂S₄ microspheres as superior noble-metal-free photocatalyst for hydrogen evolutions under visible light, *Appl. Catal. B: Environ.* 160 (2014) 552–557.
 - [36] P. Puthiaraj, W.S. Ahn, Highly active palladium nanoparticles immobilized on NH₂-MIL-125 as efficient and recyclable catalysts for Suzuki-Miyaura cross coupling reaction, *Catal. Commun.* 65 (2015) 91–95.
 - [37] H. Liu, Z.T. Jin, Z.Z. Xu, Z. Zhang, D. Ao, Fabrication of ZnIn₂S₄-g-C₃N₄ sheet-on-sheet nanocomposites for efficient visible-light photocatalytic H₂-evolution and degradation of organic pollutants, *RSC Adv.* 5 (2015) 97951–97961.
 - [38] H. Wang, X.Z. Yuan, Y. Wu, G.M. Zeng, X.H. Chen, L.J. Leng, Z.B. Wu, L.B. Jiang, H. Li, Facile synthesis of amino-functionalized titanium metal-organic frameworks and their superior visible-light photocatalytic activity for Cr(VI) reduction, *J. Hazard. Mater.* 286 (2015) 187–194.
 - [39] H. Wang, X.Z. Yuan, Y. Wu, G.M. Zeng, X.H. Chen, L.J. Leng, H. Li, Synthesis and applications of novel graphitic carbon nitride/metal-organic frameworks mesoporous photocatalyst for dyes removal, *Appl. Catal. B:Environ.* 174 (2015) 445–454.
 - [40] Y.J. Yuan, J.R. Tu, Z.J. Ye, D.Q. Chen, B. Hu, Y.W. Huang, T.T. Chen, D.P. Cao, Z.T. Yu, Z.G. Zou, MoS₂-graphene/ZnIn₂S₄ hierarchical microarchitectures with an electron transport bridge between light-harvesting semiconductor and cocatalyst: a highly efficient photocatalyst for solar hydrogen generation, *Appl. Catal. B: Environ.* 188 (2016) 13–22.
 - [41] H. Liu, Z.Z. Xu, Z. Zhang, D. Ao, Highly efficient photocatalytic H₂ evolution from water over CdLa₂S₄/mesoporous g-C₃N₄ hybrids under visible light irradiation, *Appl. Catal. B: Environ.* 192 (2016) 234–241.
 - [42] C.W. Zhao, Y.A. Li, X.R. Wang, G.J. Chen, Q.K. Liu, J.P. Ma, Y.B. Dong, Fabrication of Cd(II)-MOF-based ternary photocatalytic composite materials for H₂ production via a gel-to-crystal approach, *Chem. Commun.* 51 (2015) 15906–15909.
 - [43] S. Saha, G. Das, J. Thote, R. Banerjee, Photocatalytic metal-organic framework from CdS quantum dot incubated luminescent metallohydrogel, *J. Am. Chem. Soc.* 136 (2014) 14845–14851.
 - [44] Y.J. Chen, H. Ge, L. Wei, Z.H. Li, R.S. Yuan, P. Liu, X.Z. Fu, Reduction degree of reduced graphene oxide (RGO) dependence of photocatalytic hydrogen evolution performance over RGO/ZnIn₂S₄ nanocomposites, *Catal. Sci. Technol.* 3 (2013) 1712–1717.
 - [45] Z.W. Mei, S.X. Ouyang, D.M. Tang, T. Kako, D. Golberg, J.H. Ye, An ion-exchange route for the synthesis of hierarchical In₂S₃/ZnIn₂S₄ bulk composite and its photocatalytic activity under visible-light irradiation, *Dalton T.* 42 (2013) 2687–2690.
 - [46] Q. Li, C. Cui, H. Meng, J.G. Yu, Visible-light photocatalytic hydrogen production activity of ZnIn₂S₄ microspheres using carbon quantum dots and platinum as dual co-catalysts, *Chem. Asian J.* 9 (2014) 1766–1770.
 - [47] G.H. Tian, Y.J. Chen, Z.Y. Ren, C.G. Tian, K. Pan, W. Zhou, J.Q. Wang, H.G. Fu, Enhanced photocatalytic hydrogen evolution over hierarchical composites of ZnIn₂S₄ nanosheets grown on MoS₂ slices, *Chem. Asian J.* 9 (2014) 1291–1297.
 - [48] F.F. Shi, L.L. Chen, M. Chen, D.L. Jiang, A g-C₃N₄/nanocarbon/ZnIn₂S₄ nanocomposite: an artificial Z-scheme visible-light photocatalytic system using nanocarbon as the electron mediator, *Chem. Commun.* 51 (2015) 17144–17147.
 - [49] N. Ding, Y.Z. Fan, Y.H. Luo, D.M. Li, Q.B. Meng, Enhancement of H₂ evolution over new ZnIn₂S₄/RGO/MoS₂ photocatalysts under visible light, *APL Mater.* 3 (2015) 104417.
 - [50] F. Tian, R.S. Zhu, K.L. Song, F. Ouyang, G. Cao, The effects of amount of La on the photocatalytic performance of ZnIn₂S₄ for hydrogen generation under visible light, *Int. J. Hydrogen Energy* 40 (2015) 2141–2148.
 - [51] W.L. Yang, L. Zhang, J.F. Xie, X.D. Zhang, Q.H. Liu, T. Yao, S.Q. Wei, Q. Zhang, Y. Xie, Enhanced photoexcited carrier separation in oxygen-doped ZnIn₂S₄ nanosheets for hydrogen evolution, *Angew. Chem. Int. Ed.* 55 (2016) 6715–6719.
 - [52] X. Chen, L. Li, W.Z. Zhang, Y.X. Li, Q. Song, L. Dong, Fabricate globular flower-like CuS/CdIn₂S₄/ZnIn₂S₄ with high visible light response via microwave-assisted one-step method and its multipathway photoelectron migration properties for hydrogen evolution and pollutant degradation, *ACS Sustain. Chem. Eng.* 4 (2016) 6680–6688.
 - [53] Y.X. Li, Y.L. Hou, Q.Y. Fu, S.Q. Peng, Y.H. Hu, Oriented growth of ZnIn₂S₄/In(OH)₃ heterojunction by a facile hydrothermal transformation for efficient photocatalytic H₂ production, *Appl. Catal. B: Environ.* 206 (2017) 726–733.